

Supplementary Information

A flexible rechargeable aqueous zinc manganese-dioxide battery working at -20 °C

Funian Mo,^{†a} Guojin Liang,^{†a} Qiangqiang Meng,^{a, b} Zhuoxin Liu,^a Hongfei Li,^a Jun Fan^{*a} and
Chunyi Zhi^{*a, c}

^a Department of Materials Science and Engineering, City University of Hong Kong, 83
DachiRoad, Kowloon, Hong Kong SAR, China. Email: cy.zhi@cityu.edu.hk

^b Key Laboratory for Advanced Technology in Environmental Protection of Jiangsu Province,
Yancheng Institute of Technology, Yancheng, Jiangsu 224051, China.

^c Shenzhen Research Institute, City University of Hong Kong, Nanshan District, Shenzhen
518057, PR China.

[†] These authors contributed equally.

Methods

Preparation of EG-based waterborne anionic polyurethane acrylates (EG-waPUA)

First, 0.02 mol (10.0 g) ethylene glycol (EG, Aladdin), 0.01 mol (1.34 g) 2, 2-Dimethylol propionic acid (DMPA, Sigma-Aldrich) was added in a 250 mL flask and stirred for 2 h at 80 °C under N₂ atmosphere. Second, 10 mL acetone, 0.03 mol (6.67 g) 3-Isocyanatomethyl-3,5,5-trimethylcyclohexyl isocyanate (IPDI, Aladdin), and 80 mg catalyst Dibutyltin dilaurate (DBTDL, Aladdin) were added under stirring, and the reaction lasted for 4 h under N₂ atmosphere. After the temperature was cooled to 45 °C, 0.06 mol (3.9 g) 2- Hydroxyethyl methacrylate (HEMA, Aladdin) as end-capping reagent was added and the reaction lasted for 12 h under N₂ atmosphere. Third, 0.01 mol (0.4 g) NaOH (Bayer) was added to get salt-form reaction with carboxylic group of DMPA under 45 °C for 1 h. When the above mixture was cooled to room temperature, water was poured in under strong stirring. Finally, EG-waPUA solution was obtained by removing butanone under vacuum condition.

Preparation of anionic polyurethane acrylates/polyacrylamide (EG-waPUA/PAM) hydrogel electrolytes

The EG-waPUA/PAM hydrogels were synthesized by a radical polymerization. Firstly, EG-waPUA was added to acrylamide (AM, Aladdin) aqueous solution under stirring. The weight ratio of EG-waPUA ($G_w\%$) was 0, 8, 16, 24, 32 and 40%, respectively. Then, ammonium persulfate (APS, Aladdin) (1.5 wt% of AM) was added to the above mixed solution and bubbled with N₂ gas to get rid of oxygen. After that, the above solution was injected to a mould and evacuated to remove bubbles. Finally, the reaction was maintained under 50 °C for 12 h to form EG-waPUA/PAM hydrogels. The as-prepared hydrogels were soaked in deionized water to remove the unreacted monomers and then dried in oven at 50 °C.

Preparation of α -MnO₂/carbon nanotube (CNT) cathode

α -MnO₂/CNT nanocomposites were synthesized by a hydrothermal and coprecipitation method, using Mn(CH₃COO)₂·4H₂O, KMnO₄, and carbon nanotube (CNT) as starting materials. In a typical run, firstly, 0.50 g multi-walled CNT (Shenzhen Nanotech Port Co., Ltd.) were acid treated by refluxing the as-prepared sample in sulfuric acid (Aladdin, AR, 60%) for 6 h at 90 °C. The as-received CNT was dispersed in 40 mL deionized water and washed for 0.5 h to remove the residual acid. Secondly, 3.4 g Mn(CH₃COO)₂·4H₂O (Aladdin, AR) was dissolved in 150 mL deionized water and the dry as-prepared CNT was added into the solution under continuously stirring. Subsequently, the above mixed solution was added drop-wise slowly into an 80 mL aqueous solution dissolving 1.45 g KMnO₄ (Aladdin, AR). The mixed solution was stirred for 0.5 h and then placed in an 80 °C incubator and heated for 6 h. After that, the achieved dark brown precipitate was washed several times using deionized water and dried at 80 °C oven until the water evaporated to finally give the α -MnO₂/CNT nanocomposites.

Preparation of Zn anode

Flexible Zn electrode was prepared by a facile electrochemical deposition method on the CNT paper substrate. A typical two-electrode setup was used for Zn electroplating, in which CNT paper substrate was used as working electrode, while zinc plate (purity > 99.99%, Sigma) was used as both counter and reference electrode. Aqueous solution containing 1 mol L⁻¹ ZnSO₄ (AR grade, Sigma) and 1 mol L⁻¹ KCl (AR grade, Sigma) was used as electrolyte. Electroplating was performed at 10 mA cm⁻² for 2000 s using an electrochemical workstation (CHI 760D). The effective mass loading of zinc is about 3.0-5.0 mg cm⁻².

Characterization methods

Structural and phase characterizations of the as-prepared solid electrolytes film and electrodes were done by XRD using a Bruker D2 Phaser diffractometer with Cu K α irradiation ($\lambda = 1.54 \text{ \AA}$). The surface morphology of these samples was characterized by an environmental scanning electron microscope (ESEM, FEI/Philips XL30). The morphology and microstructure of the samples were revealed by a JEOL-2001F field-emission TEM.

Electrochemical Measurements

Cyclic voltammetry curves and electrochemical impedance spectroscopy (100 kHz to 0.1 Hz) were conducted by an electrochemical workstation (CHI 760D). Electrochemical performance of the prepared zinc manganese-dioxide batteries (Zn-MnO₂-B) were examined based on galvanostatic testing in the voltage range of 0.8-1.85 V using a Land 2001A battery testing system. The volumetric energy density (E) of the full battery was calculated by

$$E = \int_0^t IV_{(t)}dt/V \quad (1)$$

where I is the discharge current, $V_{(t)}$ is the discharge voltage at time t , dt is time differential, and V is the total volume of the whole solid-state device, which is calculated by multiplying the surface area and the thickness of the Zn-MnO₂-B.

In order to test the ionic conductivity, AC impedance Spectra measurement was executed to investigate the resistance of the hydrogel electrolyte via an electrochemical workstation (CHI 760D). The hydrogel ionic conductor was sandwiched between two plates of stainless steel with the same dimension, and was tested in the frequency ranging from 10 kHz to 0.01 Hz. After that, the ionic conductivity of polymer electrolyte can be calculated by ohmic resistance, which is approximated by the high-frequency intercept of the semi-circle in the Nyquist plot. The equation of ionic conductivity σ was calculated by

$$\sigma = \frac{l}{RA} \quad (2)$$

where σ is ionic conductivity of polymer electrolyte, and l , R , and A represent the thickness, the bulk resistance, and the test area of polymer electrolyte, respectively.

Density Functional Theory (DFT) Calculations

In order to investigate the anti-freezing mechanism of the EG-waPUA/PAM hydrogel system, DFT calculations were performed using the DFT program DMol³ in Material Studio (Accelrys, San Diego, CA). We expand the physical wave functions according to the Dmol³/GGA-PBE/DNP (3.5) basis set (3), which is comparable to 6-31G** basis sets. The Perdew-Burke-Ernzerhof (PBE) generalized gradient approximation (GGA) (2) was utilized to calculate the exchange-correlation energy. The core electrons were treated with DFT semi-core pseudo potentials. The simulation was conducted with a global orbital cutoff of 5.2 Å and a Fermi smearing of 0.005 Ha (1 Ha = 27.211 eV). Furthermore, several convergence criteria regarding the geometric optimization and energy calculation were set as below: (i) an energy tolerance of 1.0×10^{-5} Ha/atom; (ii) a self-consistent field tolerance of 1.0×10^{-6} Ha/atom; (iii) a maximum force tolerance of 0.002 Ha/Å; (iv) a maximum displacement tolerance of 0.005 Å.

Interaction energy calculation

The interaction energy (E_{int}) presents the intensity of interaction among various components in the hydrogel. It can be calculated depending on the following equation:

$$E_{int} = E_{total} - \sum E_{component} \quad (3)$$

Where E_{total} represent the whole energy, and $E_{component}$ represent the energy of between each component. The higher absolute value of the negative E_{int} indicates the stronger interaction.

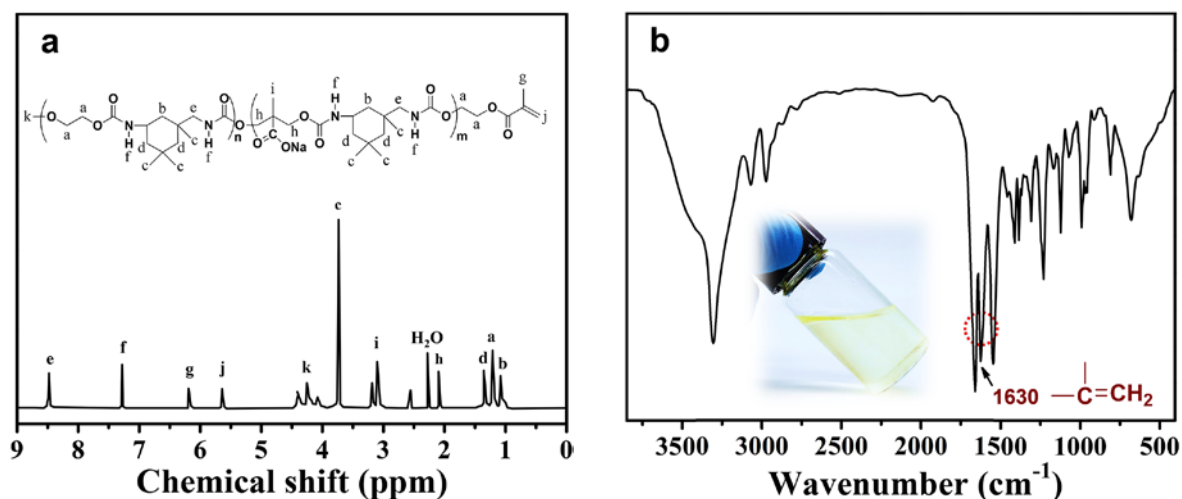


Figure S2. (a) ¹H-NMR spectra, and (b) FT-IR for the HEMA end-capped EG-based anionic polyurethane acrylates (EG-waPUA). Inset is a photograph of the aqueous dispersion.

In the ¹H-NMR spectrum (Figure S2a), the characteristic resonances of methacrylate groups, which appear at $\delta = 6.20$ ppm and 5.64 ppm, were absent after polymerization. The observed resonance peaks were also very consistent with the expected polymer structure, indicating a successful polymerization reaction. In the FT-IR spectrum (Figure S2b), the characteristic $\text{-N}=\text{C}=\text{O}$ absorption peak was absent at approximately 2260 cm^{-1} , indicating the complete reaction of isocyanate. In addition, $\text{C}=\text{C}$ stretching vibration of HEMA could be observed at approximately 1630 cm^{-1} , suggesting that the EG-waPUA polymer chains were successfully end-capped by HEMA.

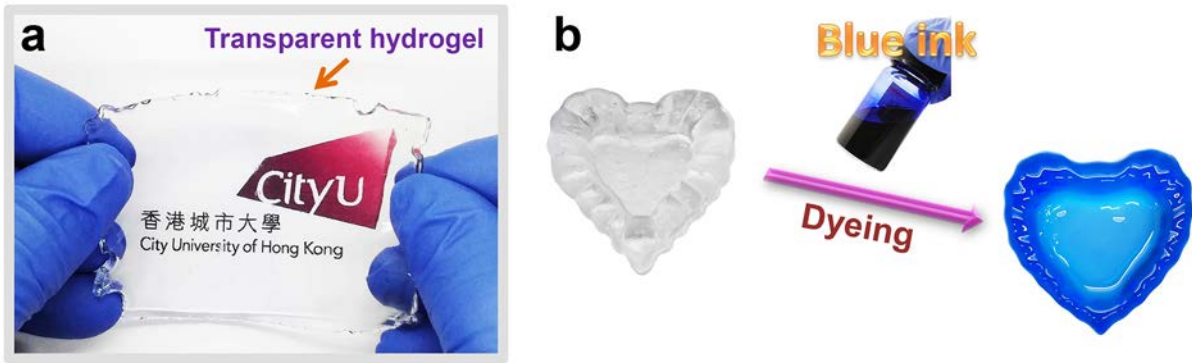


Figure S3. (a) Transparent appearance of the synthesized EG-waPUA/PAM hydrogel. (b) The dyeing process with blue ink.

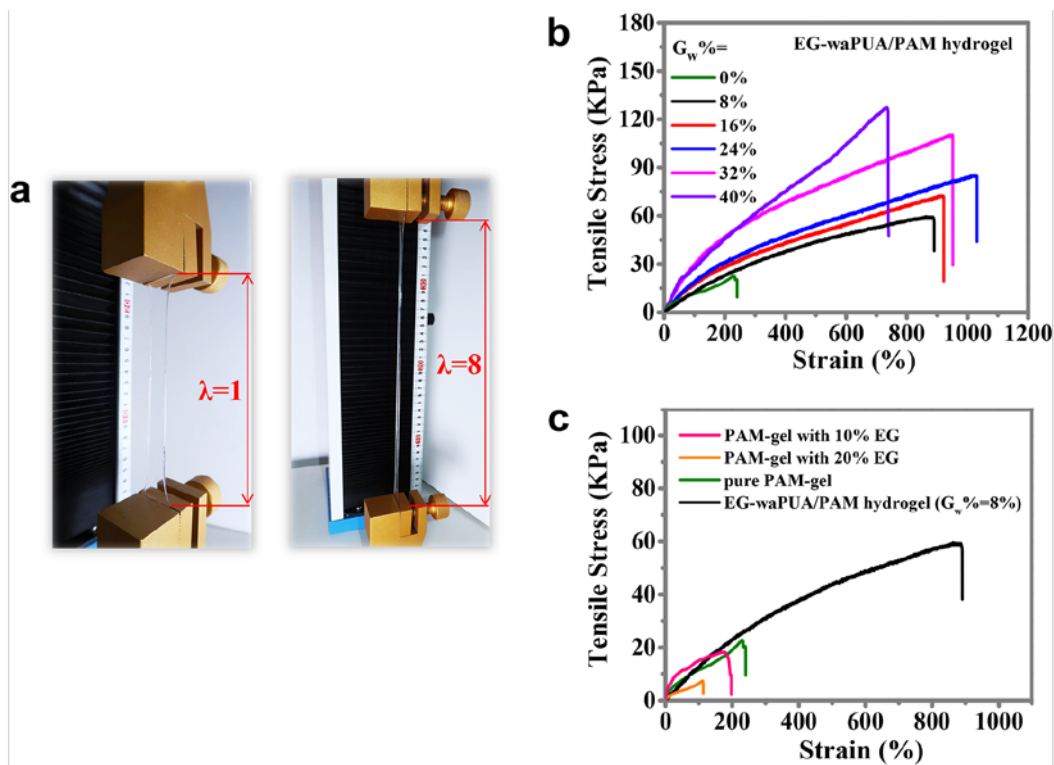


Figure S4. Tensile tests of the EG-waPUA/PAM hydrogels with various weight percentage of EG-waPUA. λ is an indicator of the hydrogel length with $\lambda=1$ indicating the original length.

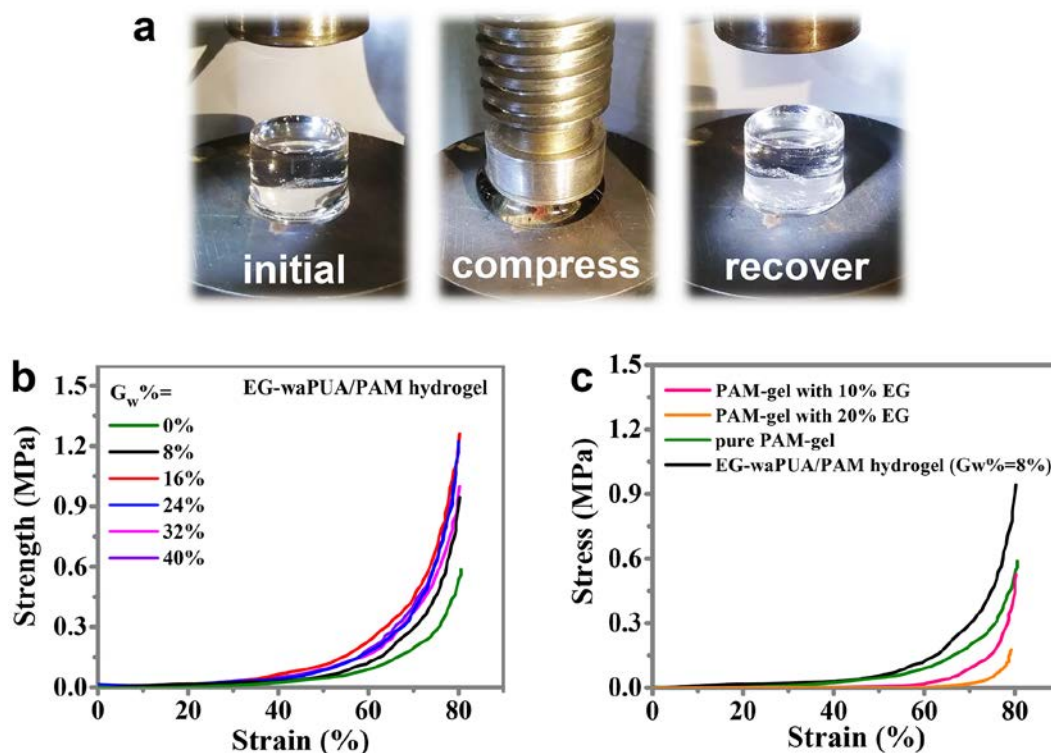


Figure S5. Compression tests of the EG-waPUA/PAM hydrogels with various weight percentage of EG-waPUA.

As shown in Figure S4, it can be observed that the tensile strength of pure PAM hydrogel was 23 KPa with 220 % elongation at break. Regarding the EG-waPUA/PAM hydrogels, the stretchability increased with the $G_w\%$ content raised from 8% to 24%, showing 58-85 KPa tensile strength, 800-1100% elongation at break, outperforming the pure PAM-hydrogel. However, further increase in the $G_w\%$ diminished the flexibility, this is because that excessive amount of EG-waPUA would lead to excessive crosslinking, and thereby decreasing the rupture strength. Similar to the tensile tests, the compression strengths of the EG-waPUA/PAM hydrogels were also remarkably improved with the increase of $G_w\%$ compared to the pure PAM-gel (Figure S5b). Furthermore, the PAM-gel formed in EG/H₂O binary solution without covalent crosslink exhibited poor mechanical performance. A possible explanation is that the non-sacrificial EG component cannot dissolve the AM monomers, thus retarding the polymerization of hydrogel (Figure S4c and S5c).

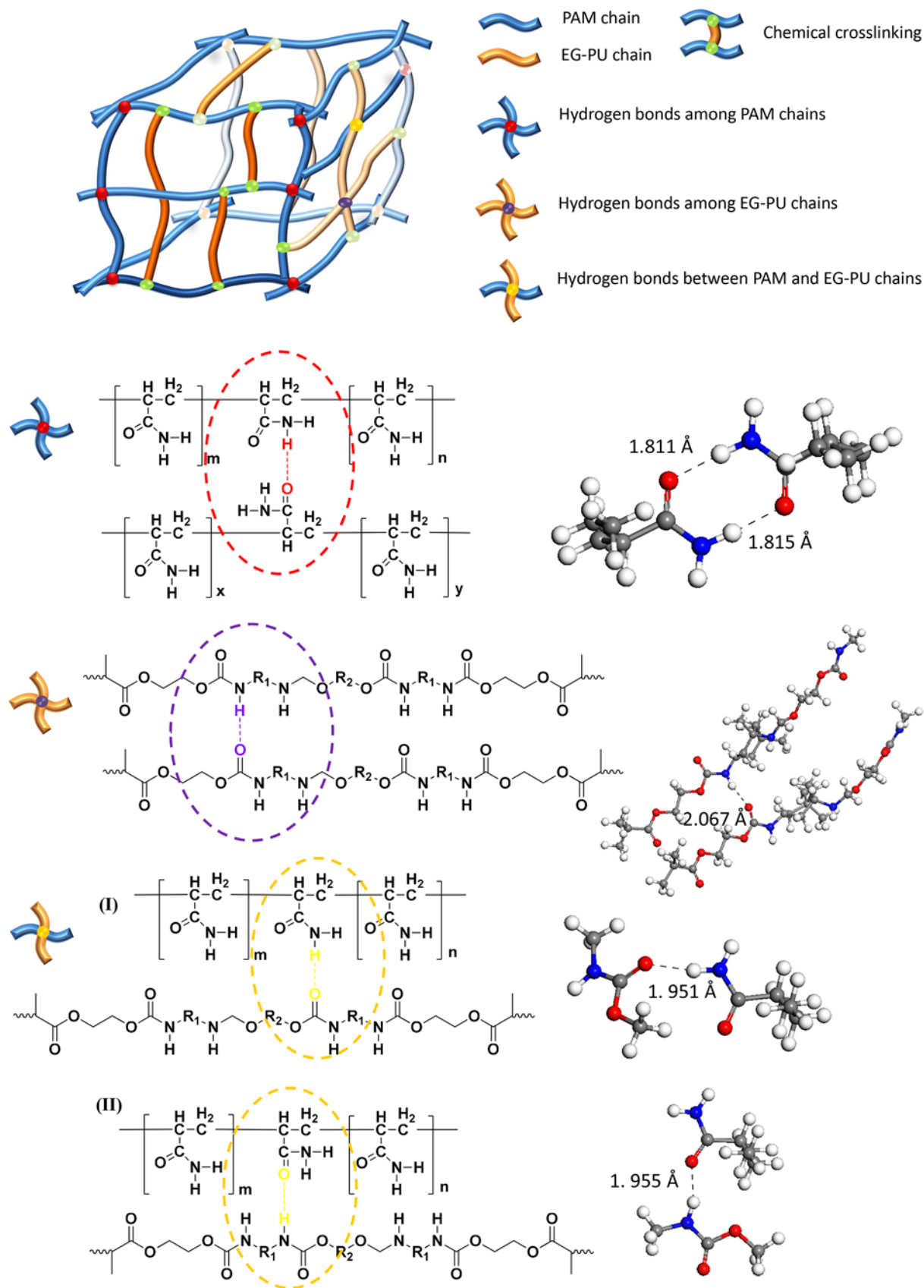


Figure S6. Schematic illustration of various crosslinking types for the EG-waPUA/PAM hydrogel.

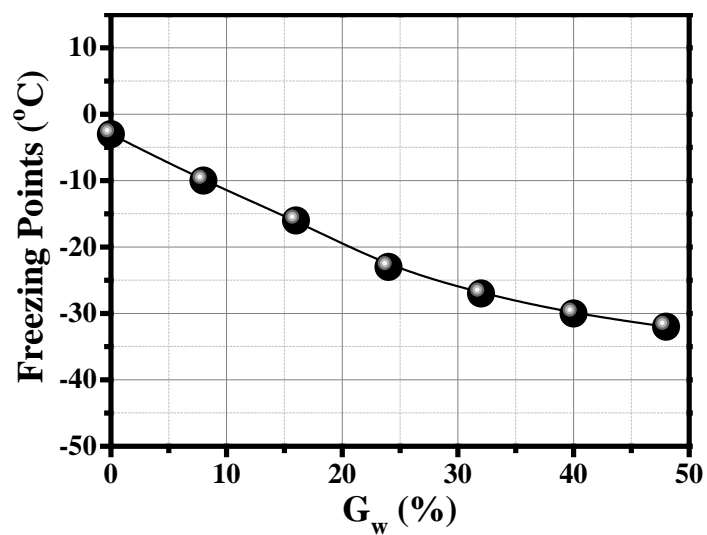


Figure S7. Freezing points of the EG-waPUA/PAM hydrogels with various weight percentage of EG-waPUA (G_w %) tested by DSC measurement.

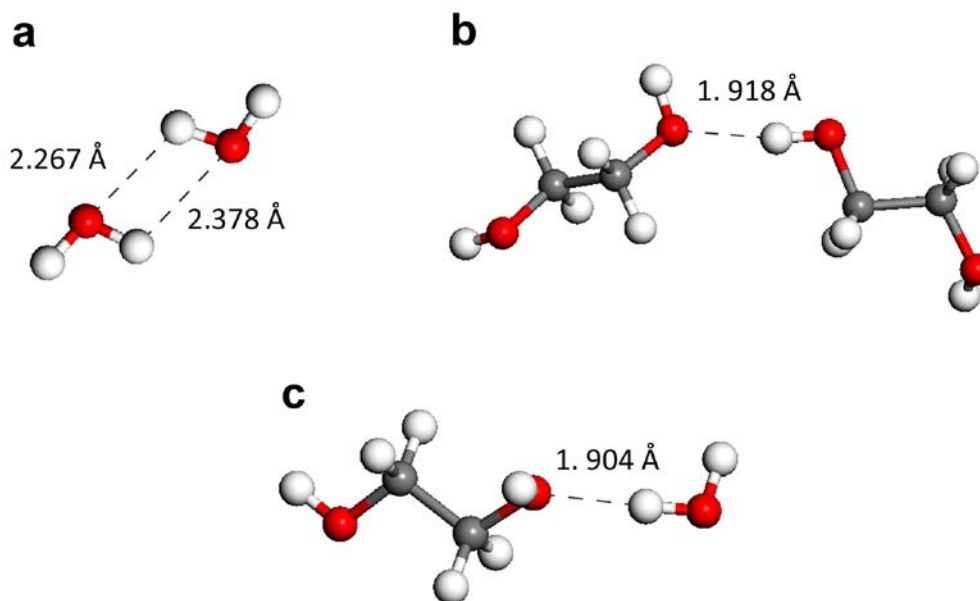


Figure S8. The interaction of water-water (W-W), ethylene glycol- ethylene glycol (EG-EG), ethylene glycol-water (EG-W).

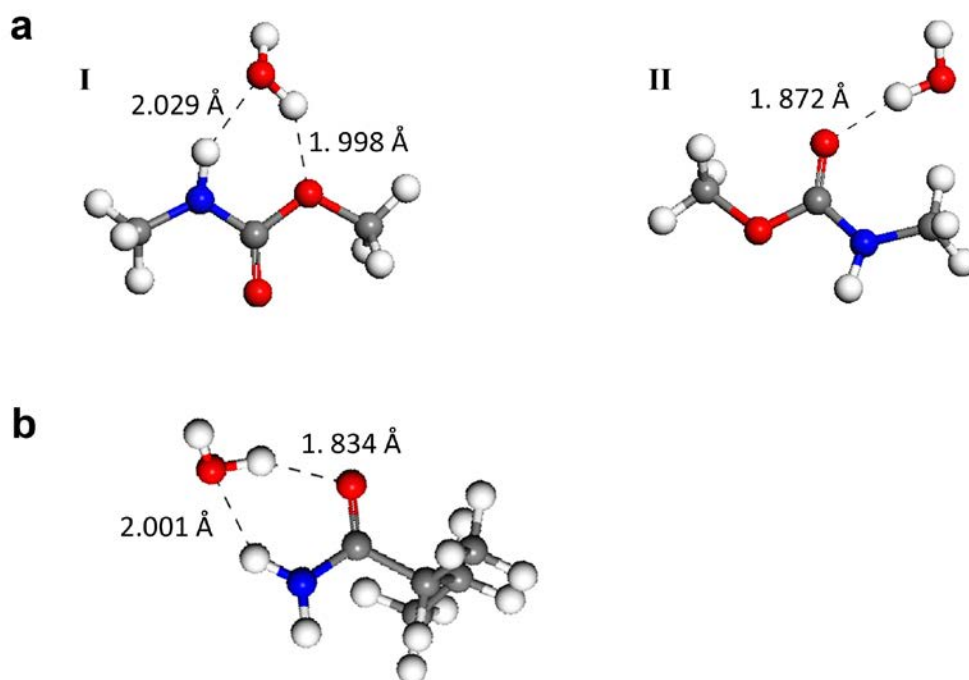


Figure S9. DFT modeling of water molecules with (a) EG-waPUA (with one unit of urethane group) and (b) PAM.

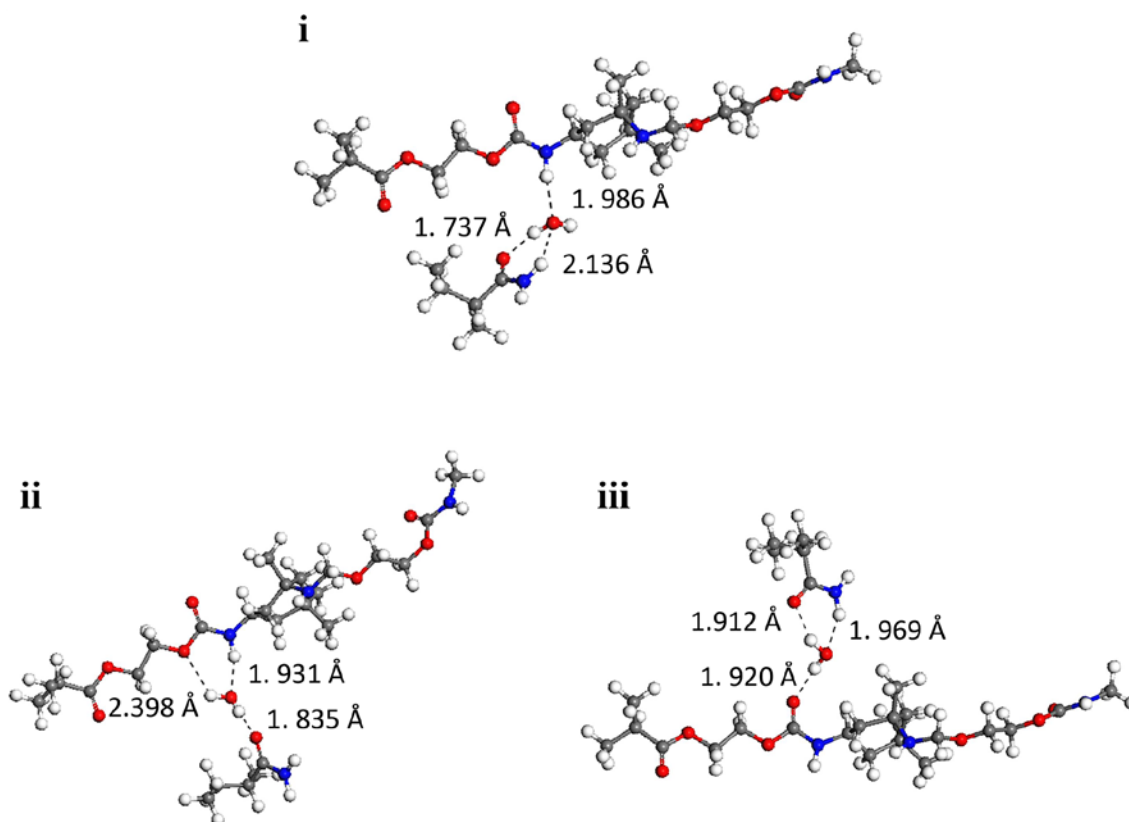


Figure S10. DFT modeling of water molecules, PAM, and EG-waPUA interacting with polymer chains *via* multiple hydrogen-bonding interactions in the AF-gel.

Table S1. DFT calculation results of the interaction energy of among various components and water molecules (W) in AF-gel polymer matrix.

Model	Interaction Energy (eV)	Interaction Energy (Kcal/mol)
W-W	-0.1660	-3.83
EG-EG	-0.2367	-5.46
EG-W	-0.2286	-5.27
(EG-waPUA)-W I	-0.2967	-6.84
(EG-waPUA)-W II	-0.2884	-6.65
PAM-W	-0.4626	-10.67
(EG-waPUA)-PAM-W i	-0.7586	-17.49
(EG-waPUA)-PAM-W ii	-0.7170	-16.53
(EG-waPUA)-PAM-W iii	-0.7570	-17.46

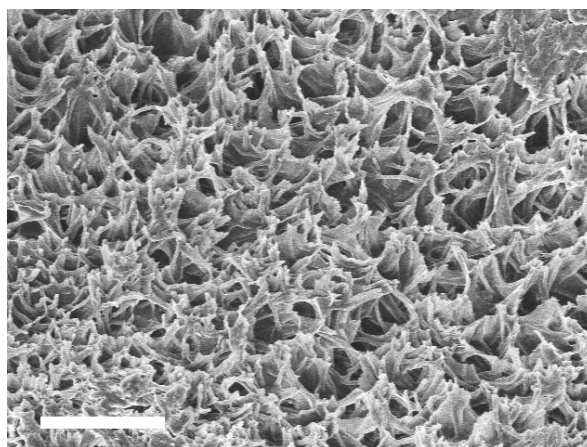


Figure S11. A SEM image of the freeze-dried AF-gel. Scale bar: 30 μm .

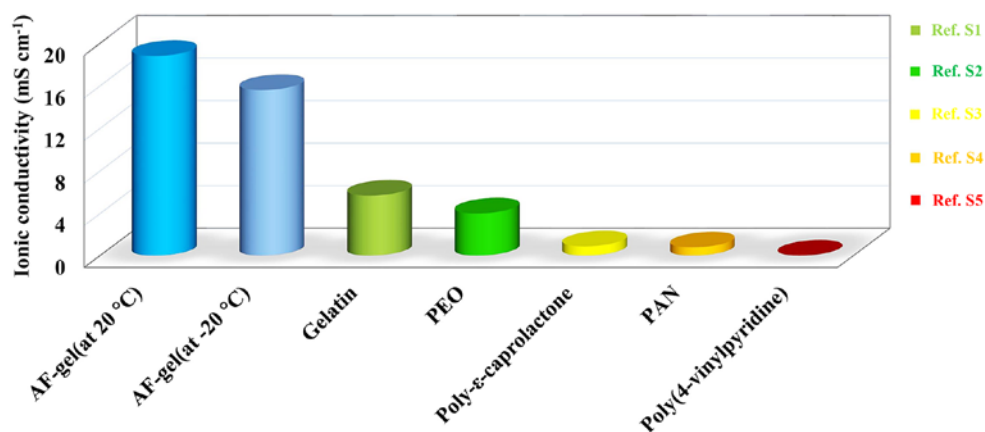


Figure S12. Comparison of AF-gel with some zinc ion conducting polyelectrolytes in terms of ionic conductivity in the literatures.¹⁻⁵

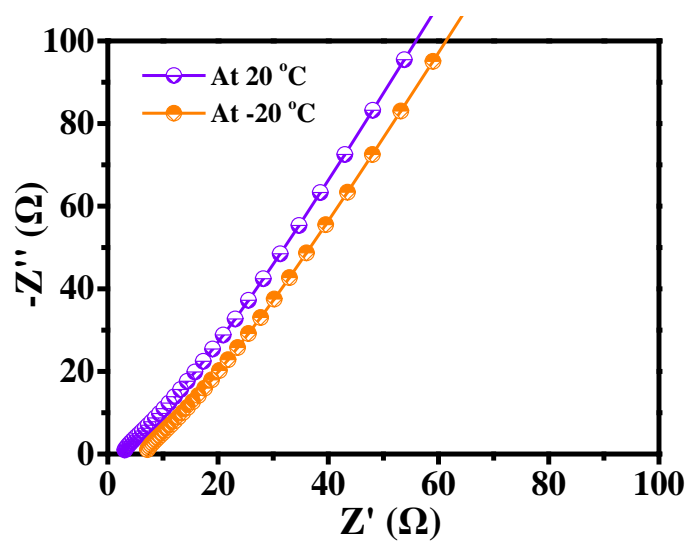


Figure S13. AC impedance spectra of the AF-gel electrolyte at 20 °C and -20 °C in the frequency range from 10 kHz to 0.01 Hz.

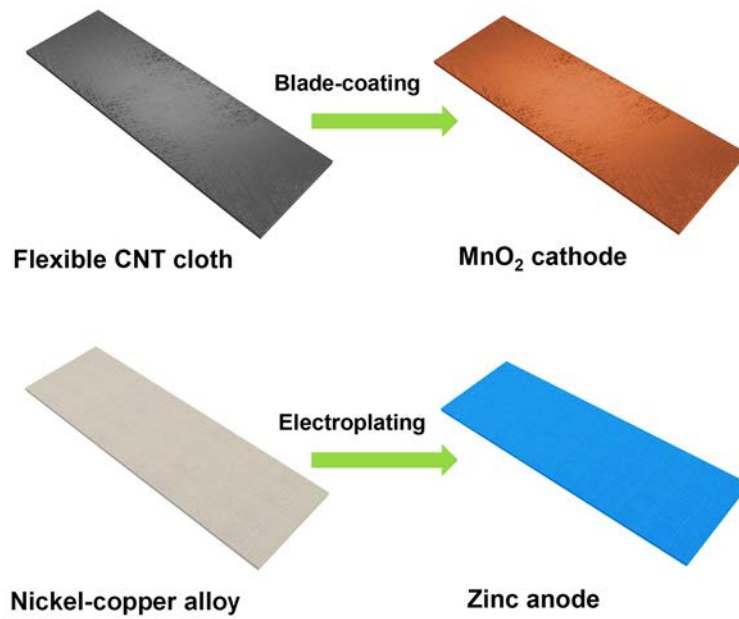


Figure S14. Schematic illustration of the preparation of flexible α -MnO₂/CNT cathode and zinc anode.

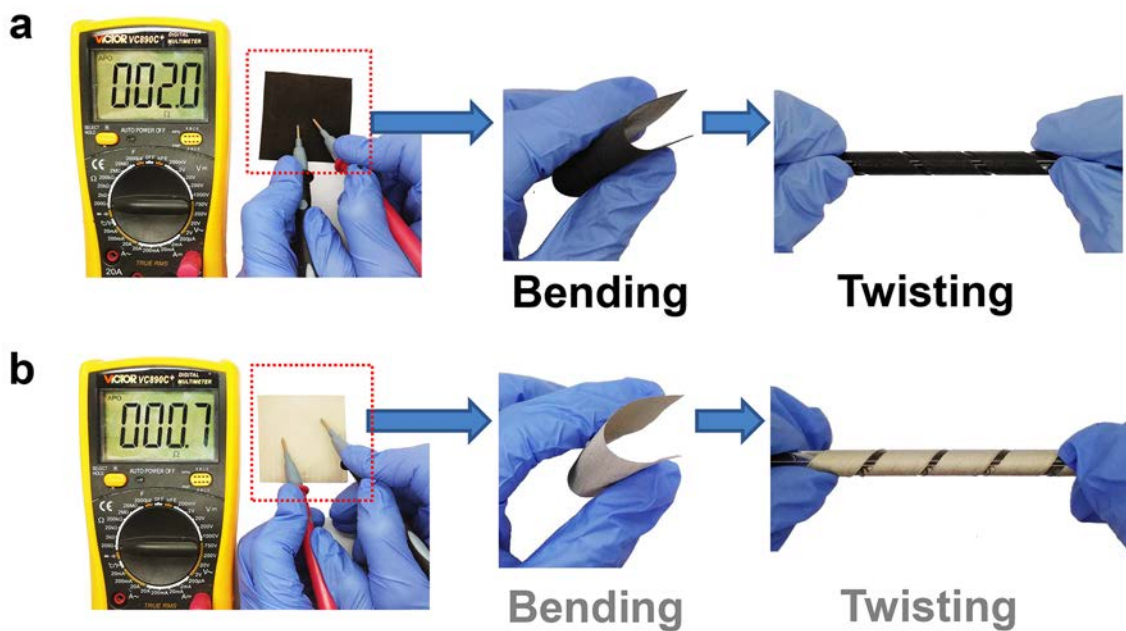


Figure S15. (a) Optical images of the flexible CNT cloth current collector with the resistance about 2.0 Ω . (b) Optical images of the nickel-copper alloy cloth current collector with the resistance about 0.7 Ω .

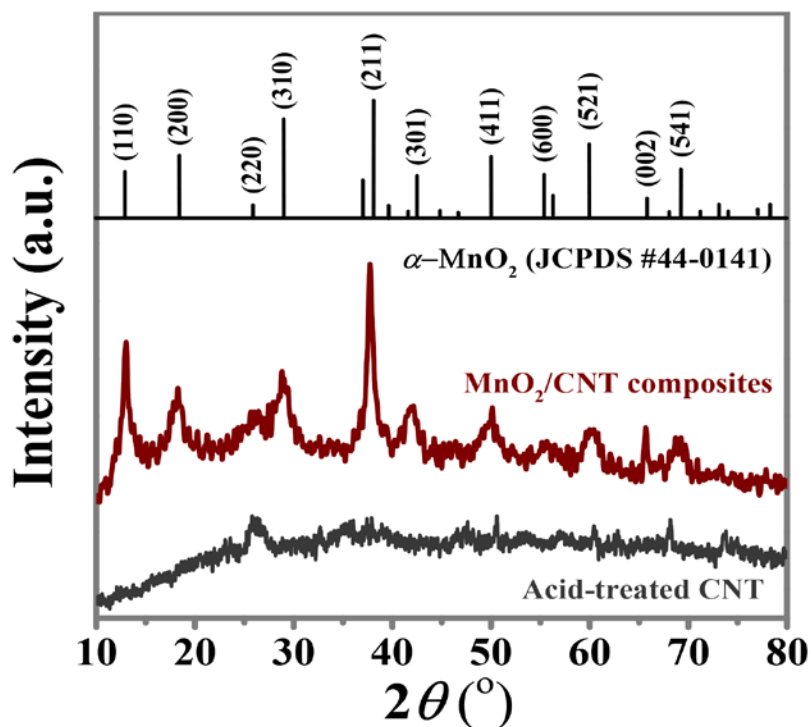


Figure S16. XRD patterns of the α -MnO₂/CNT composites and the acid-treated CNT.

Regarding the imperfectly-matched peak intensity ratio comparing with the standard sample, this phenomenon is possibly ascribed to these synergistic effects. (i) The enhanced peak at approximately 28° of MnO₂/CNT composites should also be ascribed the characteristic peak of the acid-treated CNT, as shown in the revised Figure S16. (ii) For other XRD peaks indexed to α -MnO₂ (JCPDS 44-0141), it can be ascribed to the nanocrystalline properties. According to the high resolution TEM image (Figure 3b) the crystalline α -MnO₂ exhibited the homogeneous one-dimensional nanorod structure with a lattice spacing of 0.685 nm for the (110) plane, indicating that the α -MnO₂ was highly oriented with the (110) axis as the preferred orientation. Thus, in the obtained XRD patterns, the intensity of (110) peak is of higher ratio than the standard intensity. Similar phenomenon could be observed in other nanocrystalline materials.^{6,7} (iii) In MnO₂ synthesizing process, multiple planes are formed but with a preferential growth direction of (110) crystal plane which take the dominant proportion, then other crystal planes would be affected and presented a weak and broad

feature, revealing the typical characteristic of nanocrystalline. Similar phenomenon could also be observed in the XRD pattern of MnO_2 with other phase of nanocrystalline.⁸

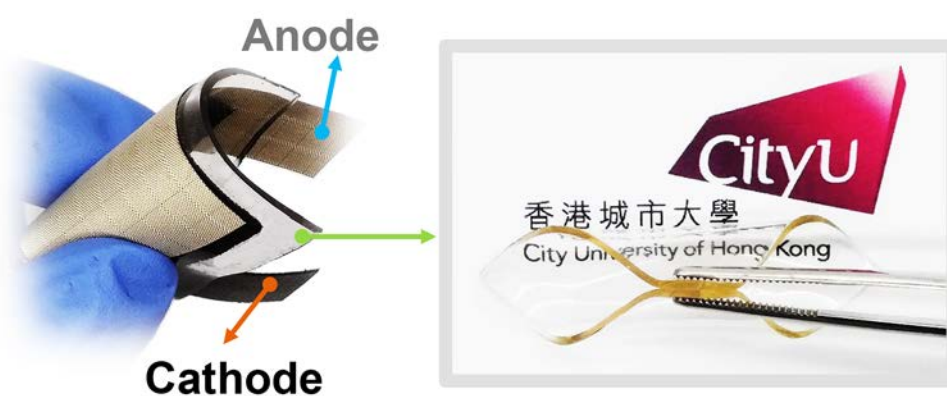


Figure S17. Top-viewed and cross-sectional photographs of the as-prepared battery comprising the AF-gel electrolyte.

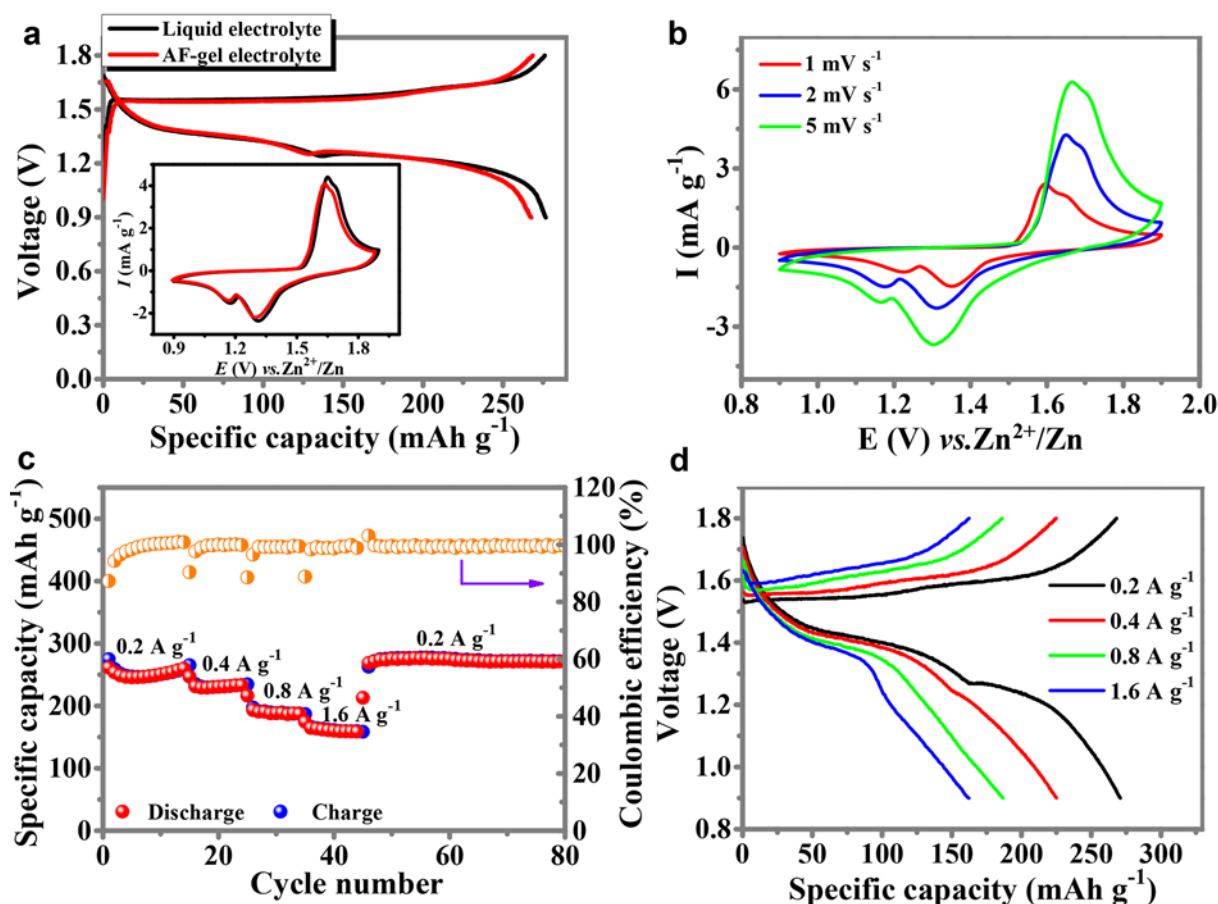


Figure S18. Electrochemical performance of AF-battery at room temperature. (a) The comparisons of tenth charge and discharge curve of Zn-MnO₂-Bs with 2 M ZnSO₄ and 0.1 M MnSO₄ liquid electrolyte and AF-gel electrolyte at 0.2 A g⁻¹. The inset is the corresponding CVs for both batteries. (b) CV curves of AF-battery at different scan rates. (d) Rate performance of AF-battery at different current densities. (e) Charge-discharge voltage profiles of the AF-battery at various current densities.

Figure S18 shows the electrochemical performance of AF-battery at room temperature. The charge-discharge curve (the tenth cycle) indicates the stable potential plateaus of the AF-battery at the current density of 0.2 A g⁻¹ at room temperature (Figure S18a), which can be confirmed by the CV profile at a scan rate of 1 mV s⁻¹ (Inset in Figure S18a). Although the over-potential between the discharge-charge potentials was a little higher than that of the battery using 2 M ZnSO₄ with 0.1 M MnSO₄ liquid electrolyte, the battery based on the

AF-gel electrolyte still delivered a high initial discharge capacity of 268 mAh g⁻¹ with a high Columbic efficiency of 99%, which was comparable to that of the aqueous electrolyte-based battery. CV curves of the AF-battery present that two distinguishable redox peaks during the discharge/charge process, respectively (Figure S18b). On one hand, the reduction peak at approximately 1.25 V was ascribed to the formation of MnOOH from α -MnO₂ accompanied with Zn²⁺ and/or H⁺ insertion for the MnO₂ cathode, and the consequent dissolution of zinc to Zn²⁺. On the other hand, the oxidization peak at around 1.7 V was due to the transformation from MnOOH to α -MnO₂, which also involving Zn²⁺ and H⁺ extraction, accompanied by the reduction of Zn²⁺ to zinc.⁸ Further discussion about the insertion mechanism of H⁺ and Zn²⁺ during the discharge process is clarified in the Figure S19.

The rate performance of the AF-battery was also measured at various current densities. The AF-battery exhibits high discharge capacities of 270, 225, 186 and 162 mA h g⁻¹ at 0.2, 0.4, 0.8 and 1.6 A g⁻¹, respectively. A discharge capacity of 275 mA h g⁻¹ was maintained after cycling back to 0.2 A g⁻¹ (Fig. S18c). All the corresponding charge-discharge curves exhibit characteristic plateaus with relatively small voltage hysteresis (Fig. S18d). These results highlight the significant structural adaptability of the AF-battery in delivering capacities at various currents.

In addition, it can be observed that the capacity of AF-gel increased higher than its initial value after rate test. This is attributed to the gradual activation of electrodes, which means: (i) The water content swollen in the hydrogel electrolyte gradually soaked the cathode material (MnO₂), and the ionic conductivity of the ions in water enhanced as the increasing interfacial compatibility between the AF-gel electrolyte and the MnO₂/CNT electrode. (ii) According to recently reported study, Chen's group utilized X-ray near edge absorption structure and X-ray absorption spectroscopy to reveal that the phase of tunnel-structured MnO₂ polymorphs gradually transfer to layered zinc-buserite during discharging process.⁹ This volume and

surface area changes significantly increase the utilization of MnO₂ materials, which allows subsequent intercalation and storage of zinc ions into the latter structure. Moreover, lower current density would facilitate this phase transition. Therefore, in the rate test, the specific capacity of AF-battery gradually increased higher than its initial value at low current density of 0.2 A g⁻¹ and maintained steady when approaching electrochemical equilibrium state.

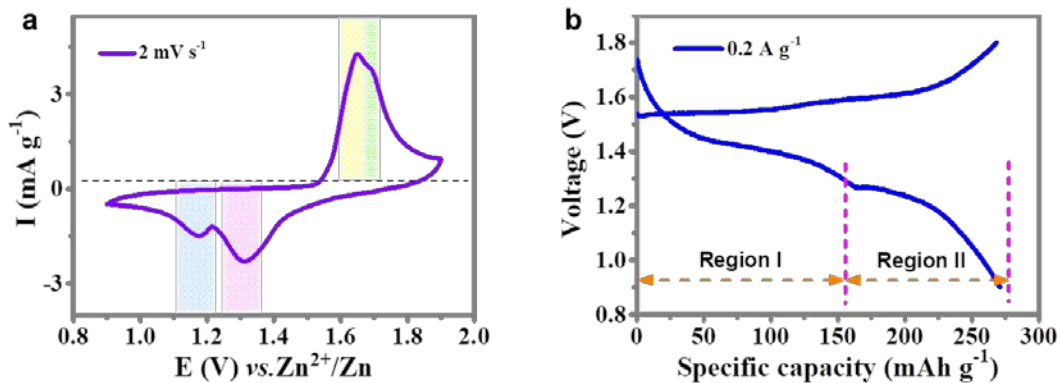


Figure S19. Insertion mechanism of H⁺ and Zn²⁺ during the discharge process. (a) CV curves of AF-battery showing two separated reduction peaks at approximately 1.25 V. (b) CCD profile showing two regions in the discharging process.

The reaction mechanism of aqueous rechargeable Zn-MnO₂ battery remains a debating topic due to diverse crystallographic polymorphs of MnO₂. According to the very recent study, Wang group used Ex situ XRD analysis to reveal the Zn²⁺ and H⁺ insertion mechanism of PANI-intercalated MnO₂ nanolayers composite during discharging process,¹⁰ which possibly can explain the two separated reduction peaks in CV curve of our AF-battery (Figure S19). It can be observed that the discharge process can be divided into two regions corresponding to two voltage plateaus. In the first region, H⁺ initially inserted into MnO₂ nanolayers, resulting in a decreased H⁺ concentration in the vicinity of the cathode. At this state, the OH⁻ concentration was not high enough for the formation of numerous amounts of zinc hydroxide sulfate, thus H⁺ insertion played the main role. With the continuous decrease of H⁺ ions, the second discharge arises, which is mainly caused by a Zn²⁺ insertion reaction and the formation of zinc hydroxide sulfate on the electrode surface increases, accompanied by the ongoing H⁺ insertion.

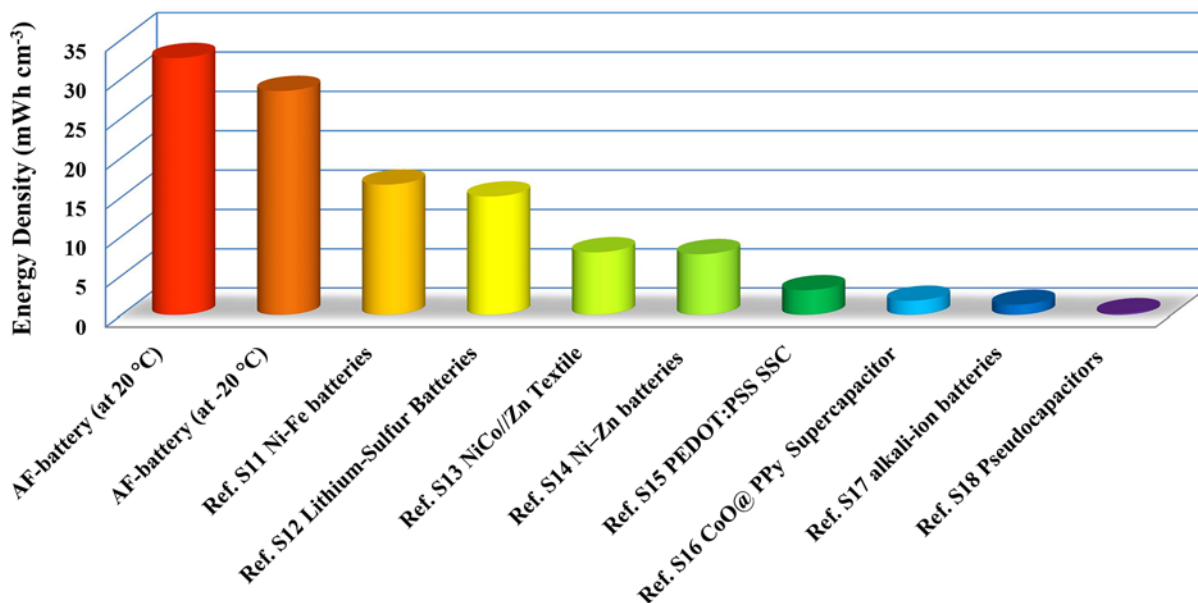


Figure S20. Comparison of volumetric energy density for present and other energy storage devices.¹¹⁻¹⁸

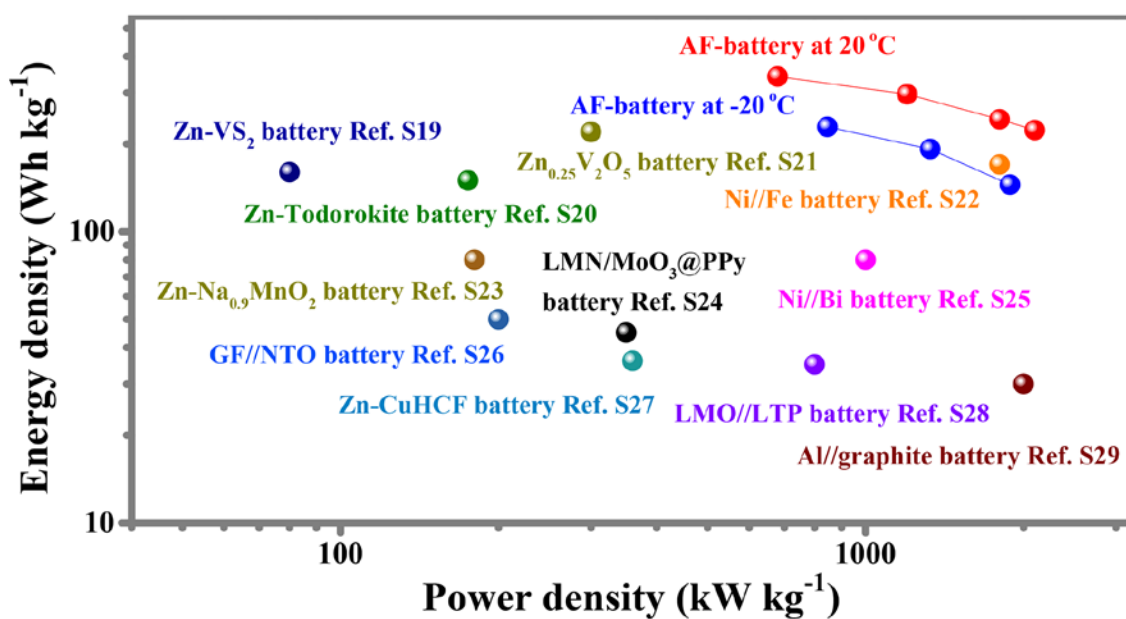


Figure S21. Ragone plots (based on the weight of cathode material) of AF-battery with other reported aqueous batteries.¹⁹⁻²⁹

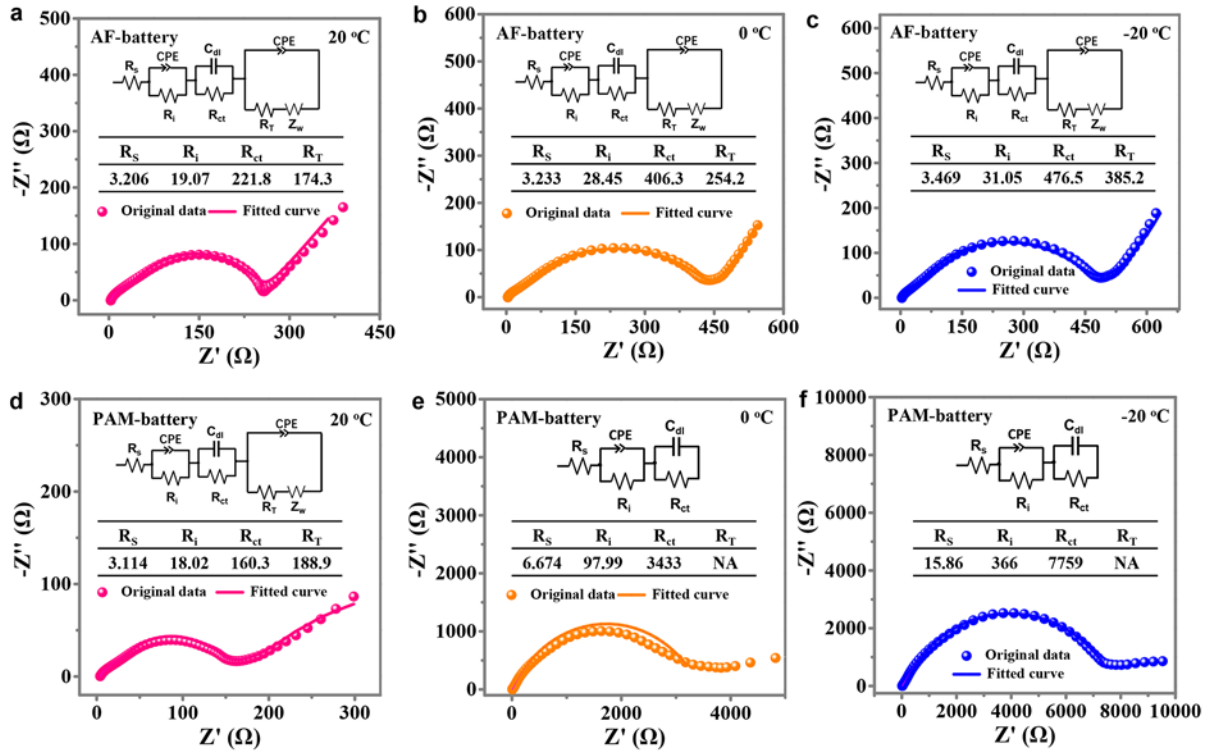


Figure S22. EIS spectra (both the original data and the fitted spectra) collected from (a)-(c) AF-battery and (d)-(f) PAM-battery at various temperatures. Each spectra is provided with the corresponding equivalent circuit for fitting and a table summarizing the value of each resistance.

In the equivalent circuit, the R_s is the series resistance of the cell;⁹ R_i is interface resistance between hydrogel electrolyte and electrode layer, R_{ct} and C_{dl} are faradic charge-transfer resistance and its relative double-layer capacitance, which correspond to the semicircle at medium frequencies;³⁰ the resistance (R_T) related to the phase change, and the Warburg impedance Z_w represents the diffusion process.³¹

In addition, it can be observed in Figure S22e and S22f that the well-fitted equivalent circuits of PAM-battery did not have the phase change resistance (R_T), which related to the phase transformation of MnO_2 from α phase to $MnOOH$, and the Warburg impedance Z_w . A possible explanation is that the high faradic charge-transfer resistance of PAM-battery significantly affected the transportation of zinc ions in the frozen hydrogel electrolyte. The

concentration of intercalated zinc in the vicinity of MnO_2 cathode was not high enough for giving rise to the phase transformation of MnO_2 from $\alpha\text{-MnO}_2$ to MnOOH , leading to the deterioration of battery performance.

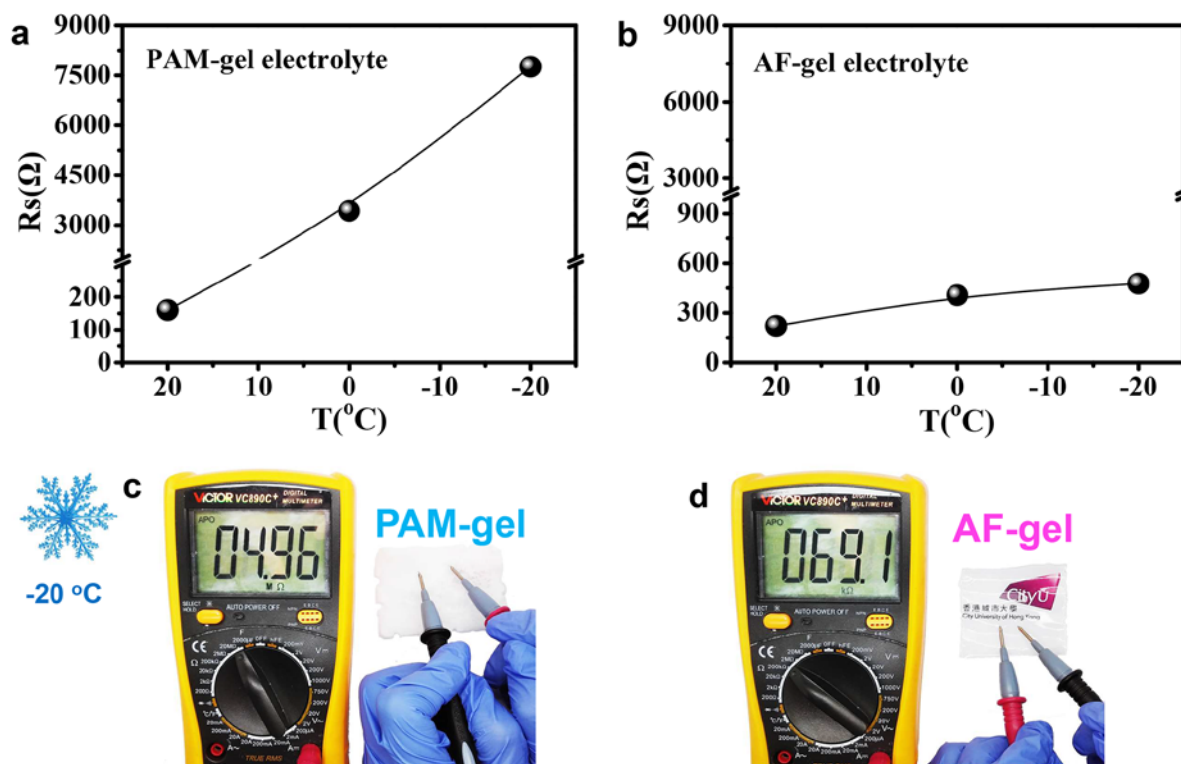


Figure S23. The statistical charge-transfer resistance of Zn-MnO₂-Bs with (a) PAM-gel and (b) AF-gel electrolyte calculated from the results of EIS (Figure S19). Electrical conductivity of (c) PAM-gel and (d) AF-gel.

As shown in Figure S20, the notable increase in the impedance of PAM-battery during cooling from 20 to 0 $^{\circ}\text{C}$ could be mainly ascribed to the loss of ionic conductivity of the frozen hydrogel electrolyte. This result was consistent with the electrical conductivity of the hydrogels tested by a multi-meter (Figure S20c and S20d). The resistance of AF-gel maintained an almost constant value at 69.1 K Ω upon cooling to -20 $^{\circ}\text{C}$, whereas the resistance of PAM-gel significantly increased to 4.96 M Ω .

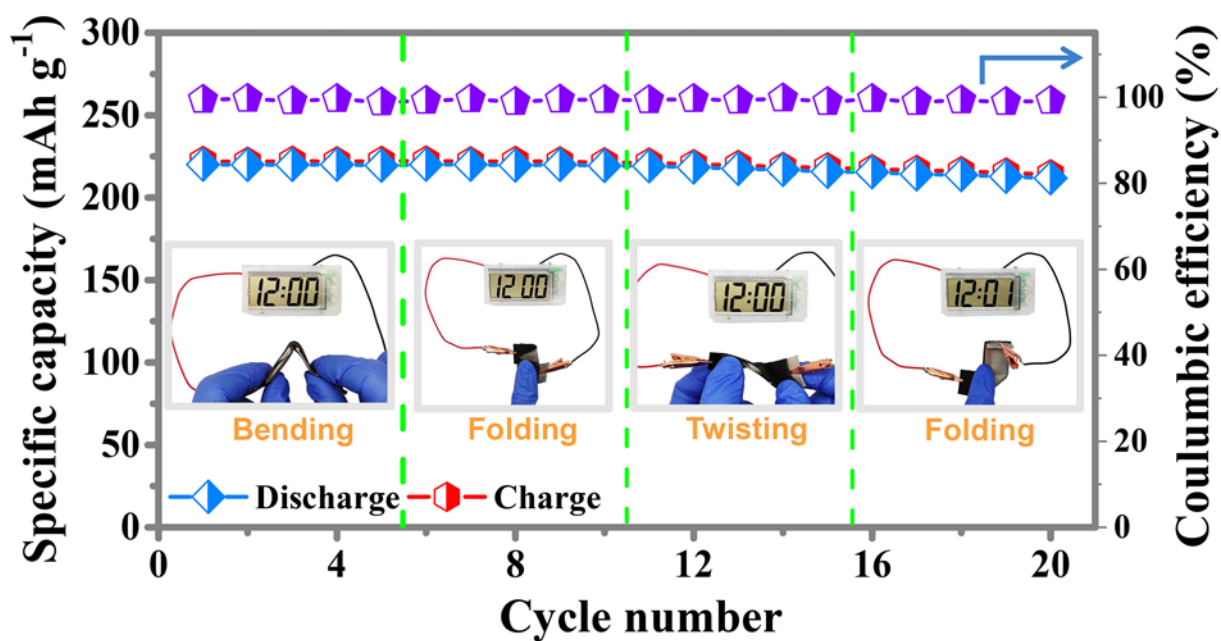


Figure S24. Cycling performance of the AF-battery at 0.4 A g^{-1} under various deformation status at room temperature.

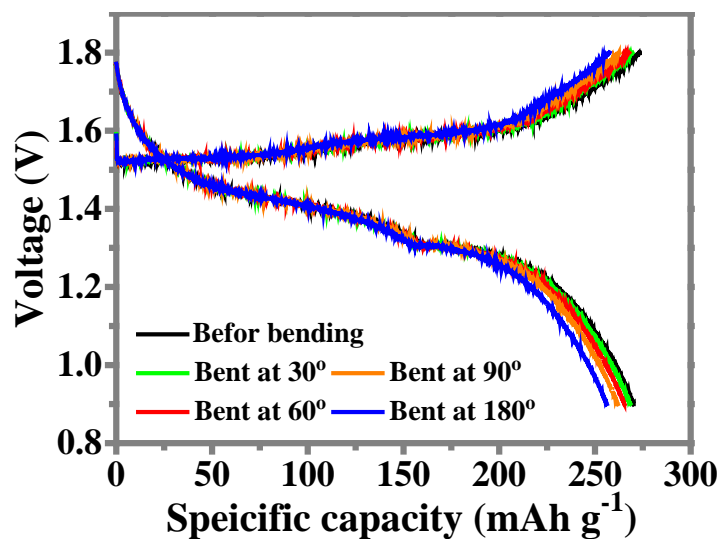


Figure S25. GCD curves of AF-battery under different bending angles at $20 \text{ }^\circ\text{C}$.

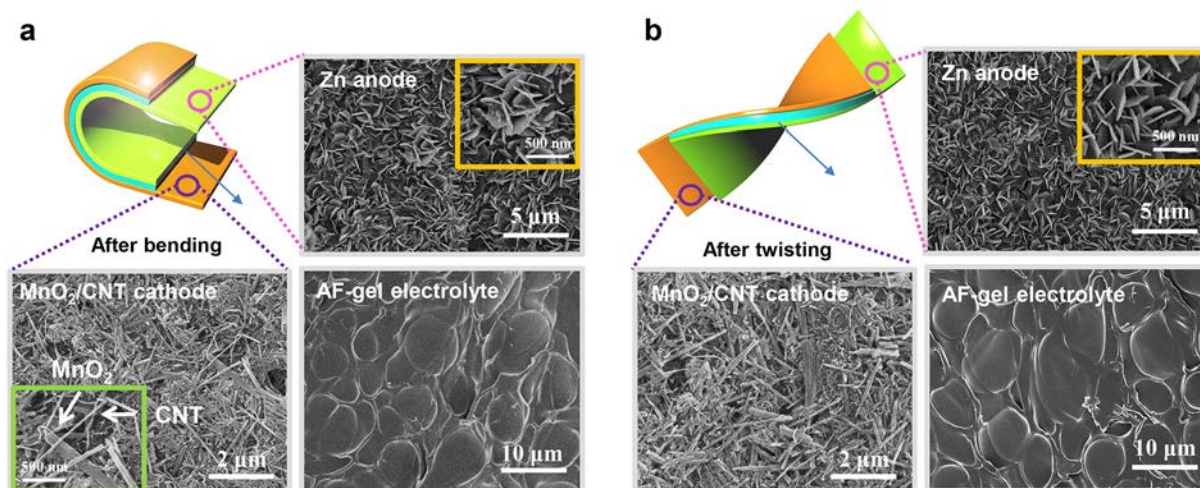


Figure S26. SEM images of the electrodes and electrolyte of AF-battery after 500 bending cycles (a) and 500 twisting cycles (b), respectively.

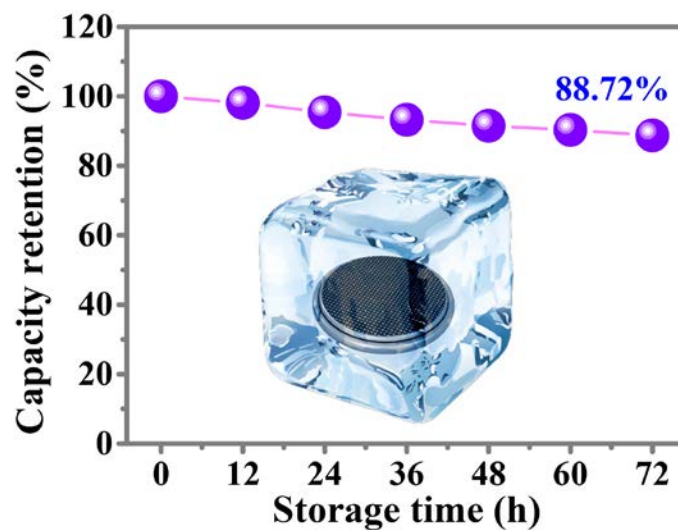


Figure S27. Capacity retention of the AF-battery sealed in a solid ice measured after different storage time at -20 °C.

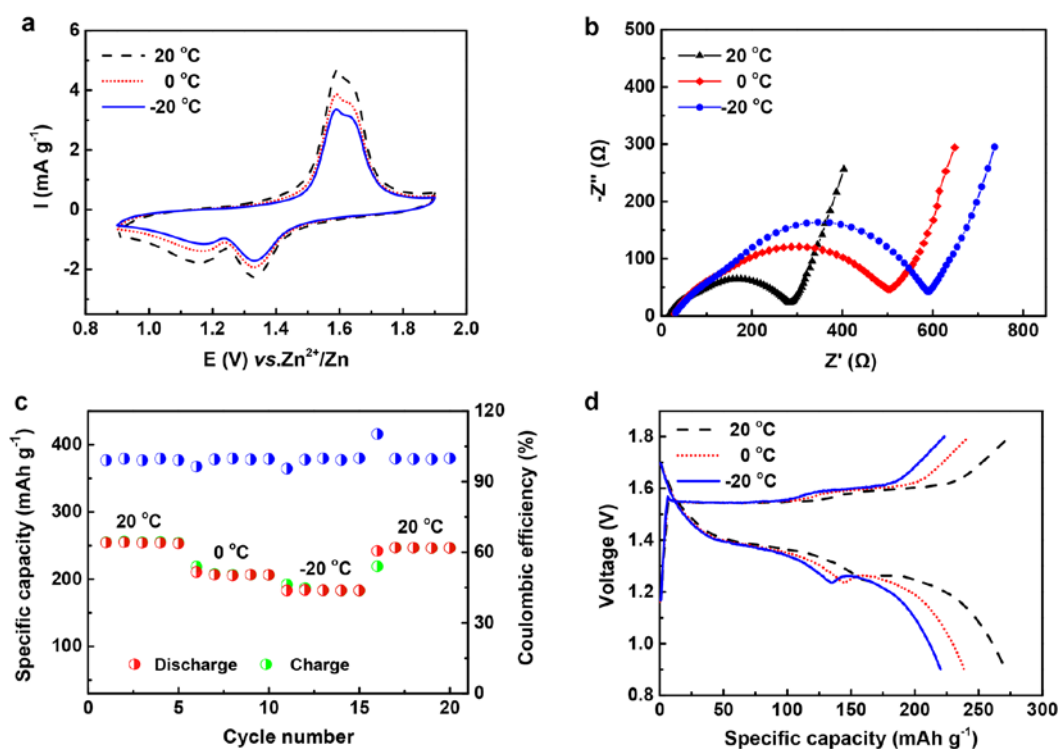


Figure S28. Electrochemical performance of the AF-battery by another independent group (Prof. Jie Yu in Harbin Institute of Technology (Shenzhen)). (a) CV curves at 2 mV s^{-1} . (b) Impedance spectra. (c) Cyclic tests and (d) corresponding GCD curves of AF-battery at 0.3 A g^{-1} under $20, 0, -20 \text{ }^\circ\text{C}$, respectively. The results are very close to electrochemical performance in our manuscript.

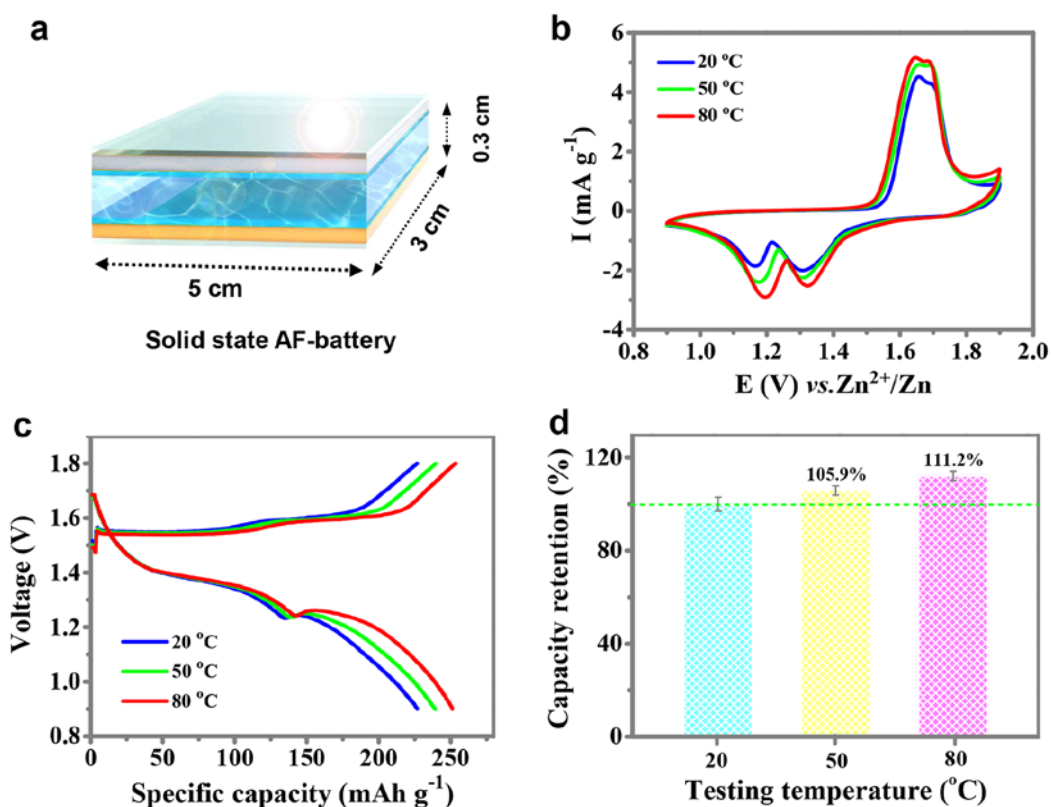


Figure S29. Electrochemical performance of AF-battery over the temperature range from 20 to 80 °C. (a) Schematic illustration of solid-state AF-batteries (size 5.0 cm×3.0 cm×0.3 cm) under the high temperature-performance measurements. (b) CV curves at 2 mV s⁻¹. (c) GCD profiles at 0.4 A g⁻¹. (d) Capacity retention of AF-battery at different temperatures.

Supplementary References

1. D. F. Vieira, C. O. Avellaneda and A. Pawlicka, *Electrochim. Acta*, 2007, **53**, 1404-1408.
2. A. Turković, M. Pavlović, P. Dubček, M. Lučić Lavčević, B. Etlinger and S. Bernstorff, *J. Electrochem. Soc.*, 2007, **154**, A554-A560.
3. K. Sownthari and S. A. Suthanthiraraj, *Express Polym. Lett.*, 2013, **7**, DOI: 10.3144/expresspolymlett.2013.46.
4. C. Kim, B. T. N. Ngoc, K. S. Yang, M. Kojima, Y. A. Kim, Y. J. Kim, M. Endo and S. C. Yang, *Adv. Mater.*, 2007, **19**, 2341-2346.
5. S. W. Kuo, C. H. Wu and F. C. Chang, *Macromolecules*, 2004, **37**, 192-200.
6. B. Liu and E. S. Aydil, *J. Am. Chem. Soc.*, 2009, **131**, 3985-3990.

7. H. G. Yang, C. H. Sun, S. Z. Qiao, J. Zou, G. Liu, S. C. Smith, H. M. Cheng and G. Q. Lu, *Nature*, 2008, **453**, 638.
8. W. Sun, F. Wang, S. Hou, C. Yang, X. Fan, Z. Ma, T. Gao, F. Han, R. Hu, M. Zhu and C. Wang, *J. Am. Chem. Soc.*, 2017, **139**, 9775-9778.
9. N. Zhang, F. Cheng, J. Liu, L. Wang, X. Long, X. Liu, F. Li and J. Chen, *Nat. Commun.*, 2017, **8**, 405.
10. J. Huang, Z. Wang, M. Hou, X. Dong, Y. Liu, Y. Wang and Y. Xia, *Nat. Commun.*, 2018, **9**, DOI: 10.1038/s41467-018-04949-4.
11. J. Liu, M. Chen, L. Zhang, J. Jiang, J. Yan, Y. Huang, J. Lin, H. J. Fan and Z. X. Shen, *Nano Lett.*, 2014, **14**, 7180-7187.
12. Z. Yuan, H. J. Peng, J. Q. Huang, X. Y. Liu, D. W. Wang, X. B. Cheng and Q. Zhang, *Adv. Funct. Mater.*, 2014, **24**, 6105-6112.
13. Y. Huang, W. S. Ip, Y. Y. Lau, J. Sun, J. Zeng, N. S. S. Yeung, W. S. Ng, H. Li, Z. Pei, Q. Xue, Y. Wang, J. Yu, H. Hu and C. Zhi, *ACS nano*, 2017, **11**, 8953-8961.
14. J. Liu, C. Guan, C. Zhou, Z. Fan, Q. Ke, G. Zhang, C. Liu and J. Wang, *Adv. Mater.*, 2016, **28**, 8732-8739.
15. Z. Li, G. Ma, R. Ge, F. Qin, X. Dong, W. Meng, T. Liu, J. Tong, F. Jiang and Y. Zhou, *Angew. Chem. Int. Ed.*, 2016, **55**, 979-982.
16. C. Zhou, Y. Zhang, Y. Li and J. Liu, *Nano Lett.*, 2013, **13**, 2078-2085.
17. S. Dong, L. Shen, H. Li, G. Pang, H. Dou and X. Zhang, *Adv. Funct. Mater.*, 2016, **26**, 3703-3710.
18. L. Hu, W. Chen, X. Xie, N. Liu, Y. Yang, H. Wu, Y. Yao, M. Pasta, H. N. Alshareef and Y. Cui, *ACS nano*, 2011, **5**, 8904-8913.
19. P. He, M. Yan, G. Zhang, R. Sun, L. Chen, Q. An and L. Mai, *Adv. Energy Mater.*, 2017, **7**, 1601920.
20. J. Lee, J. B. Ju, W. I. Cho, B. W. Cho and S. H. Oh, *Electrochim. Acta*, 2013, **112**, 138-143.
21. D. Kundu, B. D. Adams, V. Duffort, S. H. Vajargah and L. F. Nazar, *Nat. Energy*, 2016, **1**, 16119.
22. H. Wang, Y. Liang, M. Gong, Y. Li, W. Chang, T. Mefford, J. Zhou, J. Wang, T. Regier and F. Wei, *Nat. Commun.*, 2012, **3**, 917.
23. B. Zhang, Y. Liu, X. Wu, Y. Yang, Z. Chang, Z. Wen and Y. Wu, *Chem. Commun.*, 2014, **50**, 1209-1211.
24. W. Tang, L. Liu, Y. Zhu, H. Sun, Y. Wu and K. Zhu, *Energ. Environ. Sci.*, 2012, **5**, 6909-6913.
25. Y. Zeng, Z. Lin, Y. Meng, Y. Wang, M. Yu, X. Lu and Y. Tong, *Adv. Mater.*, 2016, **28**, 9188-9195.
26. B. J. Hertzberg, A. Huang, A. Hsieh, M. Chamoun, G. Davies, J. K. Seo, Z. Zhong, M. Croft, C. Erdonmez and Y. S. Meng, *Chem. Mater.*, 2016, **28**, 4536-4545.
27. T. Gupta, A. Kim, S. Phadke, S. Biswas, T. Luong, B. J. Hertzberg, M. Chamoun, K. Evans-Lutterodt and D. A. Steingart, *J. Power Sources*, 2016, **305**, 22-29.
28. J. Y. Luo and Y. Y. Xia, *Adv. Funct. Mater.*, 2007, **17**, 3877-3884.

29. M. C. Lin, M. Gong, B. Lu, Y. Wu, D. Y. Wang, M. Guan, M. Angell, C. Chen, J. Yang and B.-J. Hwang, *Nature*, 2015, **520**, 324.
30. S. Zhang, K. Xu and T. Jow, *Electrochim. Acta*, 2004, **49**, 1057-1061.
31. C. Xu, S. W. Chiang, J. Ma and F. Kang, *J. Electrochem. Soc.*, 2013, **160**, A93-A97.